Encoding a qubit in a trapped-ion mechanical oscillator

LETTER

https://doi.org/10.1038/s41586-019-0960-6

Encoding a qubit in a trapped-ion mechanical oscillator

C. Flühmann[1]*, T. L. Nguyen[1], M. Marinelli[1], V. Negnevitsky[1], K. Mehta[1] & J. P. Home[1]*

The stable operation of quantum computers will rely on error correction, in which single quantum bits of information are stored redundantly in the Hilbert space of a larger system. Such encoded qubits are commonly based on arrays of many physical qubits, but can also be realized using a single higher-dimensional quantum system, such as a harmonic oscillator[1–3]. In such a system, a powerful encoding has been devised based on periodically spaced superpositions of position eigenstates[4–6]. Various proposals have been made for realizing approximations to such states, but these have thus far remained out of reach[7–11]. Here we demonstrate such an encoded qubit using a superposition of displaced squeezed states of the harmonic motion of a single trapped $^{40}Ca^{+}$ ion, controlling and measuring the mechanical oscillator through coupling to an ancillary internal-state qubit[12]. We prepare and reconstruct logical states with an average squared fidelity of 87.3 ± 0.7 per cent. Also, we demonstrate a universal logical single-qubit gate set, which we analyse using process tomography. For Pauli gates we reach process fidelities of about 97 per cent, whereas for continuous rotations we use gate teleportation and achieve fidelities of approximately 89 per cent. This control method opens a route for exploring continuous variable error correction as well as hybrid quantum information schemes using both discrete and continuous variables[13]. The code states also have direct applications in quantum sensing, allowing simultaneous measurement of small displacements in both position and momentum[14,15].

The basic unit of quantum information is the qubit. Such a two-state system can be stored in corresponding physical systems, like the spin of an electron. However in practice, the need to correct inevitable errors requires qubits to be stored in physical systems of higher dimension, where the larger state space allows detection of errors without disturbing the stored logical information[16]. Typically, such a larger space is provided by the collective space of multiple physical qubits. Operations acting on the full state space are required in order to perform encoding, measurement and logical control[16]. An alternative approach is to use a single higher dimensional quantum system, such as a harmonic oscillator or a cavity field mode[1–3]. The use of a single system requires less resources and offers simplified control, which for microwave cavities has allowed demonstrations of logical qubits encoded and manipulated using so-called cat codes[17]. These codes are designed for correcting photon loss, which enabled extension of qubit coherence using error correction by feedback[18]. An alternative oscillator code, proposed by Gottesman, Kitaev and Preskill (GKP)[4], is based on sets of displacements generating a periodic grid with a unit cell area of $2h$ in real phase space. Compared to other oscillator codes this encoding has been shown to offer the highest correction performance, even outperforming the cat code for the photon loss channel[5]. Code states can be realized by multi-component superpositions of displaced squeezed states. These states are challenging to engineer and their preparation requires nonlinear couplings[4]. Once the qubit is encoded, full quantum state control can be achieved by combining relatively simple Gaussian transformations with measurements of the oscillator[4].

In this Letter, we experimentally demonstrate encoding, logical readout and full control of a GKP qubit in a trapped $^{40}Ca^{+}$ ion motional oscillator. We generate the code states, and measure the spatial as well as the momentum probability densities, revealing their 2D periodic grid-like non-local structure in phase space. The preparation of these 'grid' oscillator states is based on coupling the oscillator to two atomic pseudo-spin states $|0\rangle \equiv |S_{1/2}, m_j = 1/2\rangle$ and $|1\rangle \equiv |D_{5/2}, m_j = 3/2\rangle$ via state-dependent optical forces (SDF)[19], combined with post-selected internal-state readout[12]. This toolbox also allows us to read out the encoded qubit state, and by combining sets of such measurements we perform encoded state tomography. We then extend these tools using direct oscillator displacements and atomic-state rotations to implement and characterize a universal single logical qubit gate set, including non-Clifford gates teleported onto the code.

In the stabilizer formalism, a qubit code subspace is defined within a higher-dimensional Hilbert space by the action of a set of mutually commuting stabilizer operators[16]. These form the error-check operators that are measured in order to detect logical qubit errors. Such measurements should not disturb the stored information, therefore it is required that the stabilizer operators also commute with the generators of the qubit subspace, given by the Pauli operators. For a single harmonic oscillator, Gottesman, Kitaev and Preskill showed[4] that a set of stabilizer and Pauli operations can be constructed from displacements in the oscillator phase space. The operator for a displacement is $\hat{\mathcal{D}}(\alpha) = e^{\alpha\hat{a}^\dagger - \alpha^*\hat{a}}$, where α is a complex number giving the size and direction of the displacement and $\hat{a}^\dagger, \hat{a}$ are the creation and annihilation operators of the oscillator[20]. Displacement operators are in general non-commutative, following $[\hat{\mathcal{D}}(\alpha), \hat{\mathcal{D}}(\beta)] = 2ie^{i\Phi}\sin(\Phi)\hat{\mathcal{D}}(\alpha)\hat{\mathcal{D}}(\beta)$ with $\Phi = \mathrm{Im}(\beta\alpha^*)$. Displacements satisfying $\Phi = k\pi, k \in \mathbb{Z}$ commute, while for $\Phi = (2k+1)\pi/2$ they anti-commute. It follows that $\hat{X}_L \equiv \hat{\mathcal{D}}(l/2)$, $\hat{Z}_L \equiv \hat{\mathcal{D}}(i\pi/l)$ and $\hat{Y}_L \equiv \hat{\mathcal{D}}(-l/2 - i\pi/l)$ will commute with the stabilizer operators $\hat{S}_X \equiv \hat{\mathcal{D}}(l)$, $\hat{S}_Z \equiv \hat{\mathcal{D}}(i2\pi/l)$, because $\Phi = \pi$ or 0, while the two stabilizer operators have $\Phi = 2\pi$ and thus also commute. Φ is independent of the parameter l, which can thus be varied. Figure 1a gives a summary of the logical operators in phase space. The simultaneous eigenstates of $\hat{Z}_L, \hat{S}_Z, \hat{S}_X$ are the computational basis states and are periodic with respect to the three phase space shifts. The displacement operators are non-Hermitian $\hat{\mathcal{D}}(\alpha)^\dagger = \hat{\mathcal{D}}(-\alpha)$, nevertheless the action of $\hat{X}_L, \hat{Y}_L, \hat{Z}_L$ and their Hermitian conjugates are identical on the periodic code states. This ensures the correct behaviour for Pauli operators (for more details, see Methods).

The computational basis states consist of an infinite array of position eigenstates[4]. These ideal code states are unphysical, since they cannot be normalized. Approximations to these states are given by finite superpositions of displaced squeezed states[4]:

$$|0\rangle_L = \sum_{k\in\mathbb{Z}}^{\pm|k_{\max}|} c_k \hat{\mathcal{D}}(kl)\,|r\rangle,\ |1\rangle_L = \hat{\mathcal{D}}(l/2)\,|0\rangle_L \qquad (1)$$

where $|r\rangle = \hat{S}(r)\,|0\rangle$ is a squeezed vacuum state with the squeezed axis aligned with position. $\hat{S}(r) = e^{r(\hat{a}^2 - \hat{a}^{\dagger 2})/2}$ is the corresponding phase space squeezing operator, where we define the squeezing parameter r

[1]Institute for Quantum Electronics, ETH Zürich, Zürich, Switzerland. *e-mail: christaf@phys.ethz.ch; jhome@phys.ethz.ch

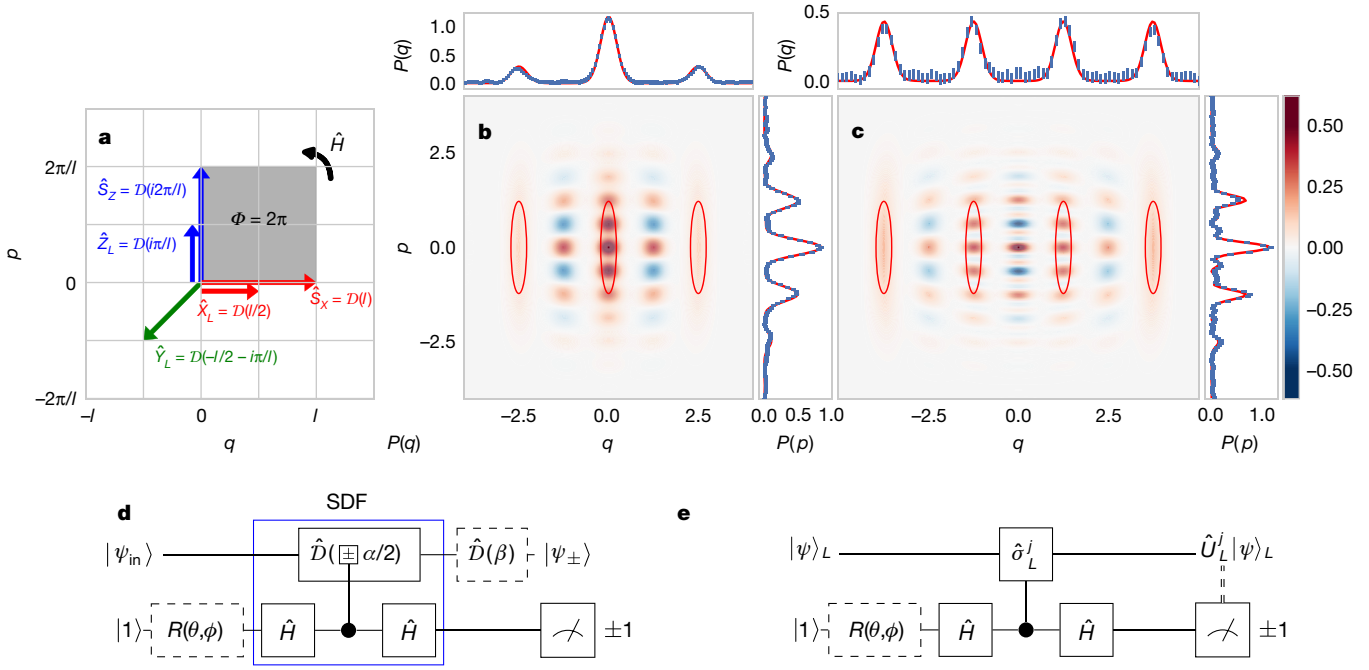

Fig. 1 | Grid state encoding and control. a, Phase space displacements for the two stabilizer operators $\hat{S}_X$, $\hat{S}_Z$ and the Pauli operators $\hat{X}_L$, $\hat{Y}_L$, $\hat{Z}_L$ showing also the relevant phase space area Φ. We define the dimensionless position $\hat{q}$ and momentum $\hat{p}$ such that for a coherent oscillator state: $\langle\alpha|\hat{q}|\alpha\rangle = \mathrm{Re}(\alpha)$, $\langle\alpha|\hat{p}|\alpha\rangle = \mathrm{Im}(\alpha)$ (see Methods). The Hadamard $\hat{H}$ operation is given by a $\pi/2$-rotation of phase space. **b**, **c**, Approximate grid code states: encoding using the non-zero coefficients $c_1 = c_{-1} = c_0/2$ and displaying the $|0\rangle_L$ state (**b**) encoding with $c_{-2} = c_{\bar{2}} = c_{\bar{1}} = c_0 = c_1$ and showing $|1\rangle_L$ (**c**). In each case we plot the Wigner function[20] (see colour bar on the right) of the grid code states obtained by a Lindblad master equation simulation of the experiment (Methods). The red ellipses show the position and r.m.s. size of the displaced squeezed wave-packets building up these grid states. The two marginal distributions $P(p)$, $P(q)$ are plotted at the corresponding sides of the central figure. Here the curve obtained by simulation is shown in red whereas blue points with error bars present measurement results (Methods)[25]. **d**, Circuit used for grid state qubit control. Operations inside the blue box are an equivalent circuit for the SDF laser pulse. Performed together with the internal-state readout, this realizes the modular measurement. The additional dashed-box operations (carrier rotation $\hat{R}(\theta,\phi)$ and phase space shift $\hat{\mathcal{D}}(\beta)$) allow teleportation of gates. Here $|\psi_{in}\rangle$ denotes an arbitrary oscillator input state and $|\psi_{\pm}\rangle$ is the output state conditioned on the measurement result ±1. **e**, As circuit **d** but for replacing the oscillator with a logical grid qubit $|\psi\rangle_L$, and using displacement settings $\alpha = l_j/2 = 2\beta$. These settings realize the controlled Pauli operator $\hat{\sigma}^j_L$, and in total the circuit implements the continuous operation $\hat{U}^j_L(\theta,\phi)$.

to be real and positive. The weight of the displaced components is given by the real pre-factors c_k. This approximate form approaches the ideal states[4,21] for larger r and k_{max}.

Experimentally, we create the code states in the axial motional mode of a single $^{40}Ca^+$ ion which has a frequency of $\omega_m \approx 2\pi \times 1.85$ MHz. We start from a squeezed vacuum state produced by reservoir engineering[22], to which we apply a sequence of modular variable measurements[7,12,23,24]. A modular measurement is implemented by a two stage process shown in the circuit in Fig. 1d excluding operations inside the dashed boxes. First (i) the ancillary internal-state qubit in $|1\rangle$ is coupled to the oscillator using a resonant internal state-dependent force implementing $\hat{\mathcal{D}}(\alpha\hat{X}/2)$ with $\hat{X}$ the internal-state Pauli operator (blue box in Fig. 1d). This is followed by (ii) detection of the internal state of the ion by resonance fluorescence. Conditioned on detecting no scattered photons, this implements the operator $\hat{E}_+ = 1/2(\hat{\mathcal{D}}(\alpha/2) + \hat{\mathcal{D}}(-\alpha/2))$ on the oscillator, producing a superposition of two displaced copies of the initial state. This process is repeated with appropriately chosen α to build up multi-component superpositions of the form given in equation (1). Figure 1b, c shows Wigner function simulations (Methods) as well as measured probability densities (Methods)[25] in both position $P(q) = \mathrm{tr}(\hat{q}\hat{\rho})$ and momentum $P(p) = \mathrm{tr}(\hat{p}\hat{\rho})$ for two approximate code eigenstates created using two rounds of modular variable measurement. Figure 1b shows an example of a $|0\rangle_L$ state consisting of three displaced components created using measurement displacements $\alpha_1 = \alpha_2 = l$, while Fig. 1c presents a four component version of $|1\rangle_L$ created using $\alpha_1 = l$, $\alpha_2 = 2l$. In both cases we choose $l \approx \sqrt{2\pi}$, which generates code states with similar modularities in q and p. To minimize sensitivity to motional dephasing, a low average phonon number $\bar{n}$ is desirable. Therefore states with a symmetric extent in q and p and with high weight close to the origin are preferable. This favours $r \approx 0.9 \approx 7.8$ dB and the three-component state on which we base our encoding in the results below. The marginals of the simulated Wigner functions provide a theory curve for the measured probability densities and match well with the data presented in Fig. 1b, c.

In order to create eigenstates of the other Pauli operators as well as implement arbitrary logical control, we perform two types of operation on the logical states. Pauli operations are simple displacements $\hat{\mathcal{D}}(\alpha)$. These are experimentally implemented by applying an oscillating voltage resonant with the trap frequency ω_m to one of our trapping electrodes[26]. The magnitude $|\alpha|$ of the displacement is set by the product of the pulse amplitude and duration, and the direction $\arg(\alpha)$ by the phase of the oscillating tone. For continuous operations, we use a modification of the modular variable measurement, which involves the full circuit shown in Fig. 1d. We use ancilla controlled displacements $\hat{\mathcal{D}}(l_j\hat{X}/4)$ along variable directions $j = X, Y, Z$ defined using $l_X = l$, $l_Z = 2\pi i/l$ or $l_Y = -l_X - l_Z$. This, together with an unconditional corrective displacement $\hat{\mathcal{D}}(l_j/4)$, which ensures remaining within the code space, realizes the controlled logical Pauli operation shown in Fig. 1e. Before the application of these pulses, a rotation of angle θ and phase $\phi(\hat{R}(\theta,\phi) = \cos(\theta/2)\mathbb{1} + i\sin(\theta/2)(\sin(\phi)\hat{X} + \cos(\phi)\hat{Y}))$ is performed on the ancillary internal-state qubit using a resonant Rabi oscillation. Conditional on the dark detection event this full circuit implements $\hat{U}^j_L(\theta,\phi) = \sqrt{2}\,(\cos(\theta/2)|+_j\rangle\langle+_j|_L + \sin(\theta/2)e^{i\phi}|-_j\rangle\langle-_j|_L)$ on the oscillator state, where $|\pm_j\rangle_L$ denotes the ±1 ideal eigenstate of $\hat{\sigma}^j_L$. In the context of error-correction codes, this transformation is often referred to as teleportation of the gate onto the code[27]. This operation

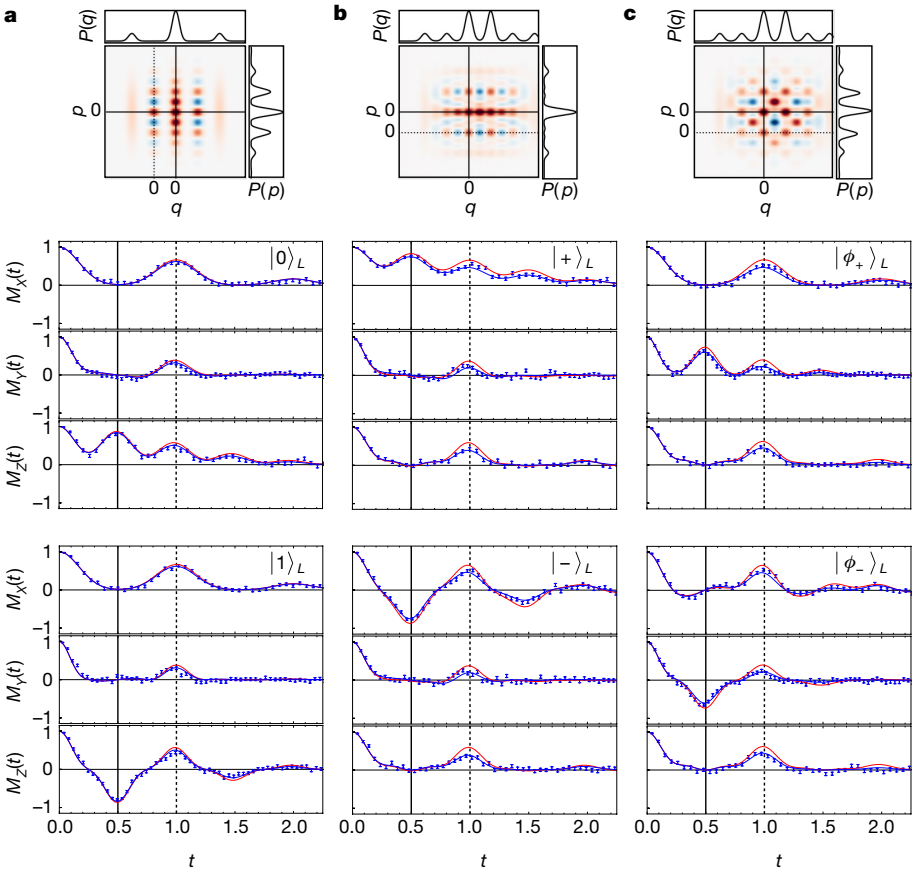

Fig. 2 | Logical readout. a, $\hat{Z}_L$ eigenstates $|0\rangle_L$, $|1\rangle_L$; **b**, $\hat{X}_L$ eigenstates $|+\rangle_L$, $|-\rangle_L$; and **c**, $\hat{Y}_L$ eigenstates $|\phi_+\rangle_L$,$|\phi_-\rangle_L$. All states were created using the settings $r \approx 0.9, l \approx \sqrt{2\pi}$ and $c_1 = c_{-1} = c_0/2$. The $\hat{Z}_L$ eigenstates are three-component superpositions whereas in **b** and **c** these are six-component superpositions given by coherent superpositions of the $\hat{Z}_L$ eigenstates' components. Middle and lower panels show state analysis measurement results. Each state is analysed by sweeping the displacement parameter $\alpha = tl_j$ along three phase space axes ($l_X = l, l_Y = -l_X - l_Z$ and $l_Z = 2\pi i/l$), and t is real and parametrizes these directions. We measure $M_j(t) = \langle \mathrm{Re}\{\hat{\mathcal{D}}(tl_j)\}\rangle$ as a function of t. The readout for $t = 0.5$ (solid vertical line) corresponds to a $\langle \hat{\sigma}_L^j \rangle$ Pauli readout, while $t = 1$ (dashed line) corresponds to the stabilizer readout $\langle \hat{S}_j \rangle$. Blue points represent measured data with the error bars given as standard errors of the mean (s.e.m.). The red line shows an analytic calculation for the chosen l, r and c_k whereas the blue line is a Lindblad master simulation including motional dephasing. Upper panels show theoretical Wigner functions of relevant motional states. In each case the -1 eigenstate is prepared from the $+1$ eigenstate via the application of a Pauli operation, thus the Wigner function of the -1 state has the same qualitative pattern but is shifted in phase space. This is accounted for in the plot by the shift of the relevant plot axes. Solid (dotted) lines are valid for $+1$ (-1) eigenstates.

is only unitary if we set $\theta = \pi/2$, resulting in a rotation $\hat{U}_L^j(\pi/2, \phi) = e^{i\phi/2}\hat{R}_L^j(\phi) = e^{i\phi/2}\exp(-i\phi\hat{\sigma}_L^j/2)$ around the j axis of the Bloch sphere[28]. However, in state preparation it is not necessary to perform unitary operations as long as the pure target state is reached, and thus we used values of $\theta = 0, \pi, \pi/2$ in the state preparations presented in Fig. 2.

Outcomes of the modular variable measurements are used to read out the logical operators and stabilizers. The internal-state readout performed in the modular measurement sequence has outcome probabilities $P(1) = \langle \psi_{\mathrm{in}} | \hat{E}_+^\dagger \hat{E}_+ | \psi_{\mathrm{in}} \rangle$ and $P(-1) = 1 - P(1)$ with the expectation value of the readout given by $\langle \hat{Z} \rangle = P(1) - P(-1) = \langle \psi_{\mathrm{in}} | \hat{Q} | \psi_{\mathrm{in}} \rangle$ where $\hat{Q} = \mathrm{Re}\{\hat{\mathcal{D}}(\alpha)\}$ and $|\psi_{\mathrm{in}}\rangle$ is the initial oscillator state. For appropriately chosen complex displacements this circuit realizes readout of the logical operators, which require only the real value since they are Hermitian for ideal code states. The readout probabilities are dependent on interference of the two displaced copies of the original state, which depends both on the state overlaps and on geometric phases[12] (Methods).

Figure 2 shows the results of such measurements performed on each of the eigenstates of $\hat{X}_L, \hat{Y}_L, \hat{Z}_L$ with non-zero coefficients $c_1 = c_{-1} = c_0/2$. Each is prepared by first creating the three-component $|0\rangle_L$, followed by appropriate displacements and teleported operations (for all settings, see Methods). Figure 2 shows additionally theoretical Wigner function plots of the created motional states. For each initialized state, we give the readout as a function of the displacement amplitude along three directions, which are parametrized as $\alpha = tl_j$ with the real number t. The periodic nature of the code states can be observed in the experimental data (blue points) presented in Fig. 2. Also shown are theory curves (red lines) together with a master equation simulation which includes the effects of motional dephasing (blue lines). We again see good agreement of the latter with our measurement. At $t = 1$ the stabilizer operators are measured. Averaging the results over the six input states yields: $\langle \hat{S}_X \rangle = 56\% \pm 1\%$ (65.8%) and $\langle \hat{S}_Z \rangle = 41\% \pm 1\%$ (59.2%). The value given in parentheses is the expectation due to the approximate nature of the code states (red lines). These measurements allow us to estimate a simultaneous average effective squeezing level of about 7.3 dB and about 5.5 dB in the two orthogonal directions[14] (see Methods for details). At $t = 0.5$, the measurements read out the logical Pauli operators, which allows us to reconstruct the logical qubit density matrix $\hat{\rho}_L = \frac{1}{2}(\mathbb{1}_L + \langle \hat{X}_L \rangle \hat{X}_L + \langle \hat{Y}_L \rangle \hat{Y}_L + \langle \hat{Z}_L \rangle \hat{Z}_L)$. We quantify the logical qubit quality by calculating the fidelity between the reconstructed state and the ideal eigenstates of $\hat{\sigma}_L^j$ given by $|\pm\rangle_L$ as $F(\hat{\rho}_L, |\pm_j\rangle_L) = \langle \pm_j | \hat{\rho}_L | \pm_j \rangle_L$. The average state creation and readout fidelity of five data sets measured over several days was 87.3% with a standard deviation between the averages of 0.7%. In this case, the finite approximation limits the achievable average fidelity to 90.8%. All the measured states are shown as red points on the Bloch sphere in Fig. 3c. Additionally, we measure the lifetime of our grid qubit by preparing $|0\rangle_L$ ($|+\rangle_L$) and monitoring the $\hat{Z}_L$ ($\hat{X}_L$) readout as a function of a preceding free evolution time. In both cases we fit exponential decays and extract timescales of $T = 3.7 \pm 0.2$ ms (3.6 ± 0.3 ms) (Methods).

Readout of logical operators allows us to examine the teleported gates $\hat{U}_L^j(\theta, \phi)$ implemented using the ancilla qubit. First we set $\theta = \pi/2$ and use the controlled $\hat{X}_L$ operation. This implements a rotation around the X axis $\hat{U}_L^X(\pi/2, \phi) = e^{i\phi/2}\hat{R}_L^X(\phi)$, with the choice of phase ϕ denoting the rotation angle. This operation applied to $|0\rangle_L$ is shown in Fig. 3a. We see that the value of $\langle \hat{X}_L \rangle$ is largely unaffected, while a clear rotation is seen in the $\langle \hat{S}_L \rangle$ and $\langle \hat{Z}_L \rangle$ signals. Figure 3b shows similar data, obtained using $\phi = \pi/2$ while varying the value of θ again using the input state $|0\rangle_L$ and the controlled $\hat{X}_L$ operation. Although this transformation is useful in state preparation it is not unitary. The states produced using both operations are shown on the Bloch sphere in Fig. 3c.

To characterize the performance of our qubit operations we use quantum process tomography. The six approximate eigenstates of $\hat{X}_L, \hat{Y}_L, \hat{Z}_L$ are used as input states, which are then subjected to the process of interest. The input density matrix $\hat{\rho}_L^{\mathrm{in}}$ as well as the output

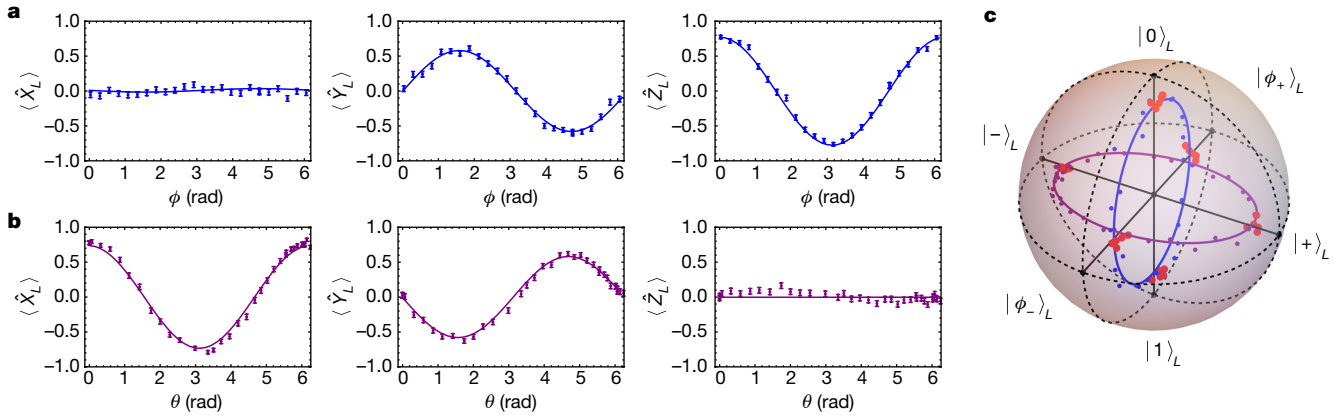

Fig. 3 | Arbitrary single-qubit operations. a, $\hat{U}_L^X(\pi/2, \phi)|0\rangle_L$, realizing a rotation around the X axis of the Bloch sphere. **b**, $\hat{U}_L^X(\theta, \pi/2)|0\rangle_L$. In **a** and **b**, $|\psi_{in}\rangle = |0\rangle_L \propto (\hat{\mathcal{D}}(-l) + 2 + \hat{\mathcal{D}}(l))|r = 0.91\rangle$ with $l = 2.36$, errors are given as s.e.m., whereas the solid line shows the Lindblad master simulation of the experiment. **c**, Summary of the continuously varied operations presented in **a** and **b** on the Bloch sphere (shown in blue and purple, respectively). Corresponding ideal operations would follow a meridian and the equator, respectively, which are given as dashed black lines. In addition, red points indicate the states shown in Fig. 2, as well as all the process tomography input states.

density matrix $\hat{\rho}_L^{out}$ are reconstructed by readout in the three Pauli bases. The process can be described by a linear map $\mathcal{E}(\hat{\rho}_L^{in}) = \hat{\rho}_L^{out} = \sum_{mn} \hat{\sigma}_L^m \hat{\rho}_L^{in} \hat{\sigma}_L^n \chi_{mn}$, which is fully defined by the complex matrix χ. From the measurement results, we obtain χ using a constrained least square optimization of the set of linear equations relating input to output states (Methods). Results for a universal set of logical gates are shown in Fig. 4. The presented set of gates is given by all three Pauli operations $\hat{X}_L, \hat{Y}_L, \hat{Z}_L$, together with the $\hat{T}_L$ gate ($\hat{R}_L^Z(\pi/4)$), and two $\pi/2$-rotations $\hat{R}_L^X(-\pi/2)$ and $\hat{R}_L^Z(-\pi/2)$ about orthogonal axes. The last three were performed by gate teleportation.

The quality of each of these operations can be evaluated by calculating the process fidelity $F_{\hat{O}} = \mathrm{tr}(\chi \chi_{id})$ between the experimentally obtained χ and the ideal logical qubit matrix χ_{id}. For the Pauli operations we find $F_{\hat{\sigma}_L^j} = 97\%$, while for the three reconstructed partial rotations around the Z and X axes we find $F_{\hat{T}_L} = F_{\hat{R}_L^Z(\pi/4)} = 92\%$, $F_{\hat{R}_L^X(-\pi/2)} = 91\%$, $F_{\hat{R}_L^Z(-\pi/2)} = 87\%$. The numerical optimization used for determining χ makes the evaluation of error bars non-trivial, and we thus forego quoting error bars here. Additionally we note that the Hadamard gate can be implemented as an update of the readout directions. By definition, the process tomography routine then gives an ideal process matrix and a process fidelity of 1.

The evaluation of the logical qubit gates given above is independent of its physical realization. Although the process tomography analysis captures the relevant information about storing and manipulating quantum information, the underlying quantum states are those of the oscillator. In practice, the change in the states of the oscillator produces a number of complications that require further study (Methods). In the work above, this includes the teleported gates generating additional grid state components, and the change in the state adjusting the logical readout levels. Sequences of Pauli gates given by phase space shifts can

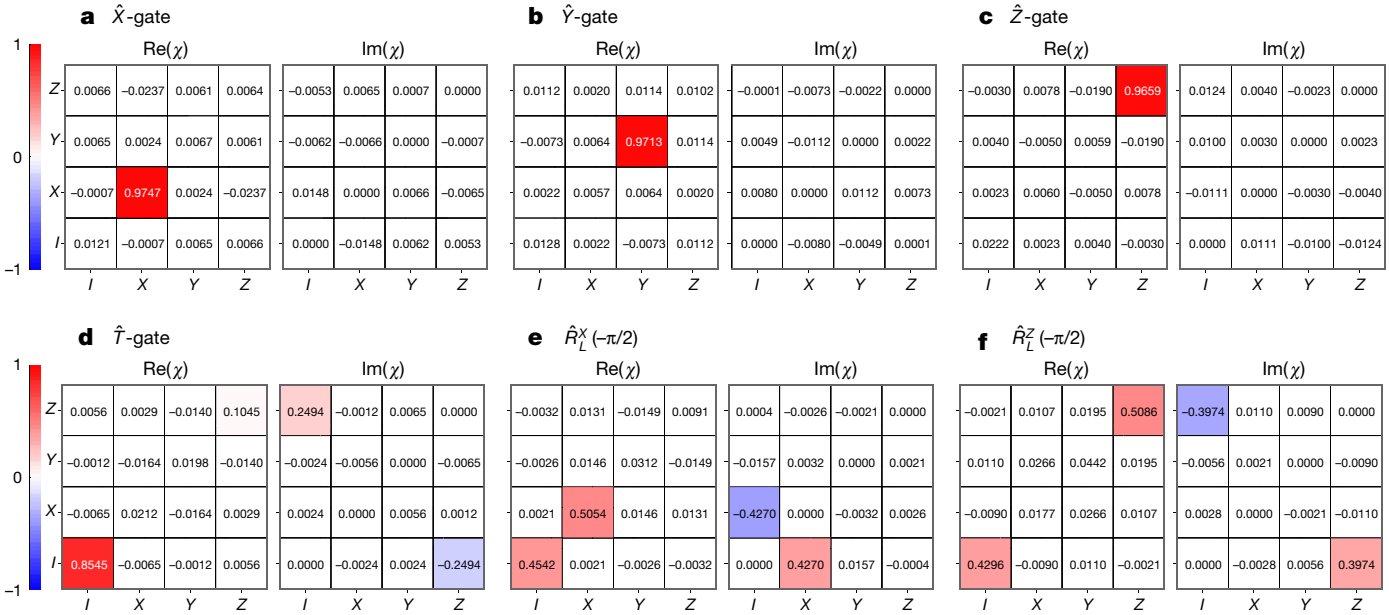

Fig. 4 | Process tomography of logical operations, characterized by the χ matrix. The reconstructed operations are as follows: **a**–**c**, Pauli gates, implemented by phase space displacements; **d**–**f**, rotations $\hat{T}_L = \hat{R}_L^Z(\pi/4)$ (**d**), $\hat{R}_L^X(-\pi/2)$ (**e**) and $\hat{R}_L^Z(-\pi/2)$ (**f**) implemented by teleportation using the internal-state qubit as an ancilla. The Hadamard operation $\hat{H}_L$ is given by an oscillator phase space rotation of $\pi/2$, which can be conveniently realized as an update to the readout direction in the classical control system. Such a permutation of readout results trivially leads to a perfect process tomography result. Each panel displays the real (Re; left) and the imaginary (Im; right) part of the χ matrix, where each entry is coloured according to the colour bar shown on the left. Red (blue) colours indicate positive (negative) values.

be optimized in order to maintain population at low $\bar{n}$ which minimizes dephasing.

Extensions to this work could include performing error correction and control of multiple encoded qubits. Multi-qubit gates could be performed by using lasers to couple two oscillation modes of one ion mediated via the internal states (Methods). A more scalable solution is to use local modes of different ions, which can be coupled using the Coulomb interaction. For resonant coupling, this generates an operation analogous to a beam-splitter, allowing a full swap of the oscillator states[29–31]. The latter could be used to realize a non-destructive readout of the grid state stabilizers by transferring quantum information to a second trapped ion which would then be decoupled from the first before fluorescence-based spin readout (see Methods). This would allow the implementation of error correction schemes using, for example, phase estimation[10,21]. To successfully concatenate grid states with qubit stabilizer codes such as the surface[32] or Toric[33] codes, an improvement in the approximation to ideal grid states would be required. Theoretical results indicate the need for squeezing levels of the order of 10–15 dB in both phase space dimensions, with the exact value dependent on the chosen error model, the architecture considered and the available quality of control. We have previously[22] prepared squeezed-vacuum states with about 12.59 dB, but improvements in both trap stability and optimization of calibration techniques would be required to achieve this for both $\hat{q}$ and $\hat{p}$ of a grid-state qubit (see Methods). While the demonstrated control provides a new route for investigating quantum error correction, the availability of two-dimensional squeezing also gives the possibility of realizing improved sensing of small phase space displacements in both position and momentum[14].

Online content

Any methods, additional references, Nature Research reporting summaries, source data, statements of data availability and associated accession codes are available at https://doi.org/10.1038/s41586-019-0960-6.

Received: 11 July 2018; Accepted: 4 January 2019;
Published online 27 February 2019.

1. Chuang, I. L., Leung, D. W. & Yamamoto, Y. Bosonic quantum codes for amplitude damping. *Phys. Rev. A* **56**, 1114–1125 (1997).
2. Michael, M. H. et al. New class of quantum error-correcting codes for a bosonic mode. *Phys. Rev. X* **6**, 031006 (2016).
3. Lund, A. P., Ralph, T. C. & Haselgrove, H. L. Fault-tolerant linear optical quantum computing with small-amplitude coherent states. *Phys. Rev. Lett.* **100**, 030503 (2008)
4. Gottesman, D., Kitaev, A. & Preskill, J. Encoding a qubit in an oscillator. *Phys. Rev. A* **64**, 012310 (2001).
5. Albert, V. V. et al. Performance and structure of single-mode bosonic codes. *Phys. Rev. A* **97**, 032346 (2018).
6. Noh, K., Albert, V. V. & Jiang, L. Improved quantum capacity bounds of Gaussian loss channels and achievable rates with Gottesman–Kitaev–Preskill codes. Preprint at https://arxiv.org/abs/1801.07271 (2018).
7. Travaglione, B. C. & Milburn, G. J. Preparing encoded states in an oscillator. *Phys. Rev. A* **66**, 052322 (2002).
8. Pirandola, S., Mancini, S., Vitali, D. & Tombesi, P. Continuous variable encoding by ponderomotive interaction. *Eur. Phys. J. D* **37**, 283–290 (2006).
9. Vasconcelos, H. M., Sanz, L. & Glancy, S. All-optical generation of states for "encoding a qubit in an oscillator". *Opt. Lett.* **35**, 3261–3263 (2010).
10. Terhal, B. M. & Weigand, D. Encoding a qubit into a cavity mode in circuit QED using phase estimation. *Phys. Rev. A* **93**, 012315 (2016).
11. Motes, K. R., Baragiola, B. Q., Gilchrist, A. & Menicucci, N. C. Encoding qubits into oscillators with atomic ensembles and squeezed light. *Phys. Rev. A* **95**, 053819 (2017).
12. Flühmann, C., Negnevitsky, V., Marinelli, M. & Home, J. P. Sequential modular position and momentum measurements of a trapped ion mechanical oscillator. *Phys. Rev. X* **8**, 021001 (2018).
13. Andersen, U. L., Neergaard-Nielsen, J. S., van Loock, P. & Furusawa, A. Hybrid discrete- and continuous-variable quantum information. *Nat. Phys.* **11**, 713 (2015).
14. Duivenvoorden, K., Terhal, B. M. & Weigand, D. Single-mode displacement sensor. *Phys. Rev. A* **95**, 012305 (2017).
15. Neumann, J. V. *Mathematical Foundations of Quantum Mechanics* (Princeton Univ. Press, Princeton, 1996).
16. Devitt, S. J., Munro, W. J. & Nemoto, K. Quantum error correction for beginners. *Rep. Prog. Phys.* **76**, 076001 (2013).
17. Heeres, R. W. et al. Implementing a universal gate set on a logical qubit encoded in an oscillator. *Nat. Commun.* **8**, 94 (2017).
18. Ofek, N. et al. Extending the lifetime of a quantum bit with error correction in superconducting circuits. *Nature* **536**, 441–445 (2016).
19. Haljan, P. C., Brickman, K.-A., Deslauriers, L., Lee, P. J. & Monroe, C. Spin-dependent forces on trapped ions for phase-stable quantum gates and entangled states of spin and motion. *Phys. Rev. Lett.* **94**, 153602 (2005).
20. Schleich, W. P. *WKB and Berry Phase* 171–188 (Wiley-VCH, Berlin, 2005).
21. Glancy, S. & Knill, E. Error analysis for encoding a qubit in an oscillator. *Phys. Rev. A* **73**, 012325 (2006).
22. Kienzler, D. et al. Quantum harmonic oscillator state synthesis by reservoir engineering. *Science* **347**, 53–56 (2015).
23. Kienzler, D. et al. Observation of quantum interference between separated mechanical oscillator wave packets. *Phys. Rev. Lett.* **116**, 140402 (2016).
24. Lo, H.-Y. et al. Spin-motion entanglement and state diagnosis with squeezed oscillator wavepackets. *Nature* **521**, 336–339 (2015).
25. Wallentowitz, S. & Vogel, W. Reconstruction of the quantum mechanical state of a trapped ion. *Phys. Rev. Lett.* **75**, 2932–2935 (1995).
26. Leibfried, D. et al. Experimental determination of the motional quantum state of a trapped atom. *Phys. Rev. Lett.* **77**, 4281–4285 (1996).
27. Knill, E., Laflamme, R. & Zurek, W. H. Resilient quantum computation: error models and thresholds. *Proc. R. Soc. Lond. A* **454**, 365–384 (1998).
28. Nielsen, M. A. & Chuang, I. L. *Quantum Computation and Quantum Information: 10th Anniversary Edition* (Cambridge Univ. Press, Cambridge, 2010).
29. Brown, K. R. et al. Coupled quantized mechanical oscillators. *Nature* **471**, 196–199 (2011).
30. Harlander, M., Lechner, R., Brownnutt, M., Blatt, R. & Hänsel, W. Trapped-ion antennae for the transmission of quantum information. *Nature* **471**, 200–203 (2011).
31. Toyoda, K., Hiji, R., Noguchi, A. & Urabe, S. Hong–Ou–Mandel interference of two phonons in trapped ions. *Nature* **527**, 74 (2015).
32. Fukui, K., Tomita, A., Okamoto, A. & Fujii, K. High-threshold fault-tolerant quantum computation with analog quantum error correction. *Phys. Rev. X* **8**, 021054 (2018).
33. Vuillot, C., Asasi, H., Wang, Y., Pryadko, L. P. & Terhal, B. M. Quantum error correction with the Toric-GKP code. Preprint at http://arxiv.org/abs/1810.00047 (2018).

Acknowledgements We thank D. Kienzler, L. de Clercq and H.-Y. Lo for important contributions to the apparatus. We acknowledge support from the Swiss National Science Foundation through the National Centre of Competence in Research for Quantum Science and Technology (QSIT) grant 51NF40-160591. We acknowledge support from the Swiss National Science Foundation under grant no. 200020_165555/1. K.M. was supported by an ETH Zürich Postdoctoral Fellowship 17-1-FEL050. The research is partly based upon work supported by the Office of the Director of National Intelligence (ODNI), Intelligence Advanced Research Projects Activity (IARPA), via the US Army Research Office grant W911NF-16-1-0070. The views and conclusions contained herein are those of the authors and should not be interpreted as necessarily representing the official policies or endorsements, either expressed or implied, of the ODNI, IARPA or the US Government. The US Government is authorized to reproduce and distribute reprints for Governmental purposes notwithstanding any copyright annotation thereon. Any opinions, findings and conclusions or recommendations expressed in this material are those of the author(s) and do not necessarily reflect the view of the US Army Research Office.

Reviewer information *Nature* thanks Alessandro Ferraro and the other anonymous reviewer(s) for their contribution to the peer review of this work.

Author contributions Experimental data were taken and analysed by C.F., using an apparatus with significant contributions from V.N., M.M., C.F., T.L.N. and K.M. The paper was written by C.F. and J.P.H., with input from all authors. Experiments were conceived by C.F. and J.P.H.

Competing interests The authors declare no competing interests.

Additional information
Extended data is available for this paper at https://doi.org/10.1038/s41586-019-0960-6.
Reprints and permissions information is available at http://www.nature.com/reprints.
Correspondence and requests for materials should be addressed to C.F. or J.P.H.
Publisher's note: Springer Nature remains neutral with regard to jurisdictional claims in published maps and institutional affiliations.

METHODS

Dimensionless position and momentum. We choose definitions of dimensionless position and momentum such that we have a simple connection to phase space: $\hat{q} = \sqrt{\frac{m\omega}{2\hbar}}\hat{q}_r$ and $\hat{p} = \sqrt{\frac{1}{2m\omega\hbar}}\hat{p}_r$; here $\hat{q}_r, \hat{p}_r$ are the real-space position and momentum operators. Using these definitions we find $\langle\alpha|\ \hat{q}\ |\alpha\rangle = \mathrm{Re}(\alpha)$, $\langle\alpha|\hat{p}|\alpha\rangle = \mathrm{Im}(\alpha)$ and $[\hat{q},\hat{p}] = i/2$. This definition simplifies working with position, momentum and displacement operators simultaneously.

Logical operations. We have argued in the main text that the action of the logical Pauli operator becomes Hermitian when acting on the ideal code states which still holds approximately for approximate code states[34]. Further, the stabilizer operators act as the identity operation on the code states. Therefore we have:

$$\begin{aligned}
&\hat{\mathcal{D}}(l/2) = \hat{X}_L \approx \hat{X}_L^{\dagger} = \hat{\mathcal{D}}(l/2)^{\dagger} = \hat{\mathcal{D}}(-l/2)\\
&\hat{\mathcal{D}}(i\pi/l) = \hat{Z}_L \approx \hat{Z}_L^{\dagger} = \hat{\mathcal{D}}(i\pi/l)^{\dagger} = \hat{\mathcal{D}}(-i\pi/l)\\
&\hat{\mathcal{D}}(-l/2 - i\pi/l) = \hat{Y}_L \approx \hat{Y}_L^{\dagger} = \hat{\mathcal{D}}(l/2 + i\pi/l)\\
&\hat{S}_X = \hat{\mathcal{D}}(l) \approx \mathbb{1}_L\\
&\hat{S}_Z = \hat{\mathcal{D}}(2i\pi/l) \approx \mathbb{1}_L
\end{aligned} \tag{2}$$

The logical Pauli operations should fulfil the relation $\hat{\sigma}_i\hat{\sigma}_j = \delta_{ij}1 + i\epsilon_{ijk}\sigma_k$; here δ_{ij} is the Kronecker delta and ϵ_{ijk} the Levi–Civita symbol. From this relation then the usual Pauli commutation and anti-commutation relations follow. We find:

$$\begin{aligned}
&\hat{X}_L^2 = \hat{\mathcal{D}}(l/2)^2 = \hat{\mathcal{D}}(l) = \hat{S}_X \approx \mathbb{1}_L\\
&\hat{Y}_L^2 = \hat{\mathcal{D}}(-l/2 - i\pi/l)^2 = \hat{\mathcal{D}}(-l - 2i\pi/l) = \hat{S}_X^{\dagger}\hat{S}_Z^{\dagger} \approx \mathbb{1}_L\\
&\hat{Z}_L^2 = \hat{\mathcal{D}}(i\pi/l)^2 = \hat{\mathcal{D}}(2i\pi/l) = \hat{S}_Z \approx \mathbb{1}_L\\
&\hat{X}_L\hat{Y}_L = \hat{\mathcal{D}}(l/2)\hat{\mathcal{D}}(-l/2 - i\pi/l) = i\hat{\mathcal{D}}(-i\pi/l) = i\hat{Z}_L^{\dagger} \approx i\hat{Z}_L\\
&\hat{X}_L\hat{Z}_L = \hat{\mathcal{D}}(l/2)\hat{\mathcal{D}}(i\pi/l) = -i\hat{\mathcal{D}}(l/2 + i\pi/l) = -i\hat{Y}_L^{\dagger} \approx -i\hat{Y}_L\\
&\hat{Y}_L\hat{Z}_L = \hat{\mathcal{D}}(-l/2 - i\pi/l)\hat{\mathcal{D}}(i\pi/l) = i\hat{\mathcal{D}}(-l/2) = i\hat{X}_L^{\dagger} \approx i\hat{X}_L
\end{aligned} \tag{3}$$

Experimental apparatus. Experiments were performed in a room temperature segmented linear Paul trap, based on a stack of laser machined and gold coated alumina wafers. A detailed description of the apparatus can be found elsewhere[35]. The ion–electrode distance is around 180 μm and we work at an intermediate magnetic field of 119 G (which is motivated by the capability of our setup to operate with beryllium as well as calcium ions simultaneously). The presented experiments rely on control via the 729 nm laser. We use monochromatic pulses for resonant carrier rotations and bi-chromatic pulses for the squeezed pumping as well as the SDF pulses, for which the relevant Lamb–Dicke parameter is 0.05. We read out our internal states using 397 nm and 866 nm laser light. 854 nm light is used for emptying the internal state $|1\rangle$ level. A resonant RF drive to our trapping electrode is used to implement unconditional oscillator shifts.

Calibration of displacement and squeezing directions. The presented experiments rely on excellent control of the oscillator phase space. This requires a stable and well calibrated motional frequency. Additionally we need to be able to reference the orientation of the squeezed state to the state-dependent force displacement direction and to the direction of the unconditional displacements which are implemented by the oscillating drive to a trapping electrode (which we refer to in what follows as 'tickling'[36]).

The SDF direction and the squeezed state orientation are both defined by the difference phase of the red and blue sideband laser components. The creation of the squeezed state and the SDF pulse use the exact same electronic and optical signal paths, thus their directions stay fixed with respect to each other. In order to match the tickle direction to that of the laser force, we create a squeezed oscillator state which we first displace using the SDF laser pulse (see Extended Data Fig. 1a, b for a schematic of the calibration in phase space). Addition of a carrier π/2-rotation before and after the SDF pulse allows the implementation of $\hat{\mathcal{D}}(\alpha\hat{Z})$[12]. Then we aim to invert this displacement using the tickling pulse. We probe whether we returned to the initially prepared squeezed state by using a bichromatic laser pulse simultaneously driving the red and the blue sideband with appropriately chosen relative amplitude and phase. This realizes the Hamiltonian $\hat{H} \propto \sigma_+\hat{U}\hat{a}\hat{U}^{\dagger} + \mathrm{h.c.}$ with $\hat{U} = \hat{S}(\xi)$. As described in detail elsewhere[22,23,37], this Hamiltonian can be viewed as a squeezed version of a motional red sideband inducing flopping between neighbouring squeezed-Fock states. The laser will not induce a change of the internal qubit state if the motion is in the squeezed ground state. Thus in cases where we succeed in inverting the unconditional displacement due to the laser we are not able to invert the qubit with the bichromatic pulse. We exploit the anisotropic nature of the squeezed state by displacing along the squeezed axis in order to calibrate the duration of the oscillating voltage (see Extended Data Fig. 1a) and along the anti-squeezed axis in order to find its phase (Extended Data Fig. 1b).

Calibration of displacement and squeezing amplitudes. The calibration of the SDF is based on monitoring the loss of overlap as a function of SDF probe time, when it is applied to either the $|0\rangle$ or $|1\rangle$ Fock states. Using a fit we extract the SDF strength. The case of the ground state is described in detail in the appendix of ref. [12].

The calibration of the squeezing parameter r is discussed in detail elsewhere[22]. After pumping into the squeezed ground state we apply a blue sideband pulse and observe the internal state population as a function of pulse time. The blue sideband couples neighbouring Fock states with a Rabi frequency which scales as $\sqrt{n+1}$[26]. Fitting the observed oscillations to the expected dynamics for a squeezed state using a floated variable r allows us to estimate the amount of squeezing.

Motional frequency calibration. We calibrate the motional frequency of $2\pi \times 1.85$ MHz to an accuracy of around 10 Hz (95% confidence interval). Frequency drifts of up to 1.8 Hz min^{-1} are observed, but often these are much lower. Nevertheless we recalibrate the motional frequency at least every 5 min. A quick, accurate and robust frequency calibration is thus required. Our calibration method is shown schematically in Extended Data Fig. 1c. We first ground state cool the ion's motion and then apply an oscillating tickle voltage with frequency $\omega_m + \delta$ to one of our trapping electrodes, where δ denotes a small detuning from the correct frequency ω_m. This tone prepares a coherent state of $|\alpha| \approx 4.3$. This is followed by a wait time of around 1.4 ms, after which we apply a second oscillating voltage with opposite phase to the first pulse. The final motional state is then probed with a red sideband pulse. In the case $\delta = 0$, the motional state returns to the ground state after this sequence and thus the red sideband will not be able to invert the internal state of the ion. For $\delta \neq 0$, the ion ends in an excited motional state, and the electronic state has a non-zero probability of being inverted by the red sideband pulse. Using a squeezed initial oscillator state and a squeezed basis probe pulse[22] gives a geometrical advantage for this calibration. Nevertheless the method using the ground state proved to be experimentally more robust and was therefore used. Our calibration feature takes about 30 s to measure and is well fitted with a Lorenzian line shape $A/[1 + (2(\omega - \omega_m)/w)^2]$ with a width $w \approx 2\pi \times 170$ Hz. This calibration method is very similar to the one recently presented in ref. [38]. It differs mainly in the initial motional state used and the use of a final red sideband probe pulse.

Decoherence of motional states. The decoherence of the motional oscillations in our trapped-ion system is primarily thought to be caused by noise in the trapping potentials. Such noise can fluctuate on various timescales and to characterize its exact spectrum is a demanding experimental task. The measured heating rate of our trap is around 10 quanta per s for the secular frequencies used in the experiment. Over many years we have observed coherence times for a superposition of the Fock states $(|0\rangle + |1\rangle)/\sqrt{2}$ of between 15 ms and 40 ms (early measurements are reported in ref. [35]). Frequent frequency calibrations (every five minutes) indicate the presence of slow fluctuations of the order of ±20 Hz between calibration measurements. We find that the combined effect of our noise is typically well accounted for by simulating the experiments with a purely dephasing Lindblad operator $(\sqrt{\Gamma}(\hat{a}\hat{a}^{\dagger} + \hat{a}^{\dagger}\hat{a}))$ with $\Gamma = 7 - 15\ \mathrm{s}^{-1}$. The close agreement of such a simulation with the experiment can be seen in the main part of Fig. 2 and also in the results in Figs. 1, 3. But we can not consistently simulate all experiments using such a Lindblad term; for example, we observe discrepancies between our lifetime measurements and the simulations.

Effective squeezing of grid state qubits. Grid states can be considered in some senses to be squeezed in both phase space directions. We can characterize this through an effective squeezing parameter which is defined through the measurement of the stabilizer operators as[14]:

$$\Delta_j \approx \sqrt{\frac{1}{\pi}\ln\left(\frac{1}{\langle\hat{S}_j\rangle^2}\right)} \tag{4}$$

If we consider the $\hat{S}_Z = \hat{\mathcal{D}}(\sqrt{2\pi}\,i)$ stabilizer acting on the vacuum state squeezed along the position direction, then we recover a relation to the standard squeezing parameter r as $\Delta_Z^2/2 = \mathrm{e}^{-2r}$. Thus we can more generally state the effective squeezing in dB for any state as $10\log_{10}(2/\Delta_j^2)$. The values of our stabilizer readouts on grid states are $\langle\hat{S}_X\rangle = 0.56 \pm 0.01$, $\langle\hat{S}_Z\rangle = 0.41 \pm 0.01$ from which we calculate ~7.3 dB and ~5.5 dB of effective squeezing, respectively.

To assess the improvement to our experiment required to reach a value of 10 dB squeezing or better in both directions we use numerical simulations. As an example, we simulate the creation and stabilizer readout of a logical $|1\rangle_L$ using the following assumed conditions:

(1) Doubling the current laser power, leading to $\sqrt{2}$ improvement in our Rabi frequencies.

(2) Shortening the control system decision time of each modular measurement from 50 μs to 10 μs.

(3) Adding one more round of modular measurement for the initial state preparation and increasing the squeezing to $r = 1.4$. This leads to the approximate preparation of the state $|1\rangle_L \propto [\hat{\mathcal{D}}(-1.5l) + 3\hat{\mathcal{D}}(-0.5l) + 3\hat{\mathcal{D}}(0.5l) + \hat{\mathcal{D}}(1.5l)]\,|r = 1.4\rangle$ with $l = \sqrt{2\pi}$.

(4) Reducing our dephasing rate in the Lindblad operator $\sqrt{\Gamma}(\hat{a}\hat{a}^\dagger + \hat{a}^\dagger\hat{a})$ to $\Gamma = 2\ \mathrm{s}^{-1}$.

This simulation leads to effective squeezing of ~10.05 dB and ~10.30 dB. However this does not include infidelities due to imperfect squeezed state preparation or mis-calibrations of the SDF pulse.

Measured probability densities. Measurements of probability densities have been previously used in trapped ion experiments[39–41]. Using these methods, the Fourier transform of the probability density is assessed experimentally. We zero-pad our data before performing the discrete Fourier transform and use bootstrapping in order to obtain error bars[42].

Logical state readout. The readout is based on the non-commutativity of phase space displacements $\hat{\mathcal{D}}(\alpha)\hat{\mathcal{D}}(\beta) = \mathrm{e}^{2i\mathrm{Im}(\alpha\beta^*)}\hat{\mathcal{D}}(\beta)\hat{\mathcal{D}}(\alpha)$ and interference of the grid states with themselves. This is explained in the following for the l_Z readout direction and on a $|\psi_{\mathrm{in}}\rangle = |0\rangle_L = \sum_k c_k\hat{\mathcal{D}}(kl)\,|r\rangle$ state. The modular measurement probability is given by $P(\pm1) = \langle\psi_{\mathrm{in}}|\hat{E}_\pm^\dagger\hat{E}_\pm|\psi_{\mathrm{in}}\rangle$, which is given by the overlap of the un-normalized post-measurement state of the oscillator $\hat{E}_\pm|\psi_{\mathrm{in}}\rangle$ with itself. This post-measurement state consists of two displaced copies of the input state $|0\rangle_L$. One copy is displaced towards negative momentum by $\alpha/2$ while the other copy is displaced in the opposite direction. Only components originating from the same initial grid state component k, that is, $\hat{\mathcal{D}}(kl)\,|r\rangle$ have significant overlap. For each of these the non-commutativity of the displacement operators leads to a different phase factor. Using these relations we find $P(+1) \approx 1/2(1 + \sum_k \cos(2l_Z tkl)\langle r|\hat{\mathcal{D}}(il_Z tkl)|r\rangle)$ from which $P(-1) = 1 - P(+1)$ follows. We can observe this functional form in Fig. 2a. The initial increase of t leads first to different phases between the various terms in the sum and the readout signal drops. At $t = 0.5$, which corresponds to readout of $\hat{Z}_L$, the phases of each term are multiples of 2π and ideally would completely rephase. Due to the finite squeezing the overlap $\langle r|\hat{\mathcal{D}}(tl_Z)|r\rangle = \exp(-|tl_Z|^2\,\mathrm{e}^{-2r})$ is reduced. The next revival occurs at $t = 1$ corresponding to readout of the stabilizer operator, where we see that the overlap dropped even further. Using $|1\rangle_L$ as an input state, the different position of the squeezed components changes the geometric phase factors by an offset $2\pi t$, leading to a negative revival for $t = 0.5$. Similar arguments can be made for the readouts in the other directions. For example, in the l_X case components originating from neighbouring grid state components will overlap and these overlaps will add up constructively or destructively dependent on the initial relative phase between these components. Here revivals will be reduced relative to an ideal grid state due to the finite number of displaced components.

State tomography. We reconstruct logical grid states via readout in the three logical Pauli bases $\hat{\rho}_L = \frac{1}{2}(\mathbb{1}_L + \langle\hat{X}_L\rangle\hat{X}_L + \langle\hat{Y}_L\rangle\hat{Y}_L + \langle\hat{Z}_L\rangle\hat{Z}_L)$. Any measurement will yield an expectation value in the range $[-1,1]$ and thus lead to a valid density operator. However it is worth noting that state tomography does not assess how well we are in the code space. An illustrative example would be the measurement of $\langle\hat{X}_L\rangle = \langle\hat{Y}_L\rangle = \langle\hat{Z}_L\rangle = 0$. This result could be obtained either from a fully mixed logical grid qubit state given by $\hat{\rho}_L = \frac{1}{2}\mathbb{1}_L$, or from a motional state which has fully decohered. In the first case the stabilizer values would both be $+1$ while for the latter the stabilizer readout would give zero.

As was seen in the previous section the logical readout levels are limited by the underlying approximate code states. In particular they depend on how well the states are true eigenstates of the two stabilizer operators $\hat{S}_X, \hat{S}_Z$. The readout of $\hat{S}_X$, $\hat{X}_L$ improves with a higher number of squeezed components, while more initial squeezing improves the $\hat{S}_Z$ and $\hat{Z}_L$ readouts. We optimized the experimental code states in such a way that readouts of $\hat{Z}_L$ and $\hat{X}_L$ are limited at a similar level. In turn the $\hat{Y}_L$ readout is limited by both the number of components and the squeezing and is thus expected to be lower.

Pulse sequences. In Extended Data Table 1 all pulse sequences used to create the eigenstates of $\hat{X}_L, \hat{Y}_L, \hat{Z}_L$ are summarized. Each of the state creation sequences starts with the preparation of a squeezed vacuum state $|r\rangle = \hat{S}(r)\,|0\rangle$ with $r \approx 0.9$ corresponding to ~7.8 dB of squeezing[22]. The squeezed state serves then as the input to a sequence of two modular measurements (Mod)[12]. In almost all preparations we make the two sequential modular measurements with identical displacements reading out the observable $\hat{Q} = \mathrm{Re}\{\hat{\mathcal{D}}(\approx\sqrt{2\pi})\}$ implemented by ~38 μs of SDF laser pulse. This creates the desired $|0\rangle_L$ with $c_1 = c_{-1} = c_0/2$ and any other coefficient $c_k = 0$. The other states are created from $|0\rangle_L$ using appropriate Pauli operations and teleported gates. For the data presented in Fig. 2 we used Pauli operations in order to transform from the $+1$ eigenstate to the -1 eigenstate, while in performing process tomography we created the -1 eigenstates directly from $|0\rangle_L$ using gate teleportation. These sequences lead to $p \approx 3/8$ success probability to create $|0\rangle_L$ and $|1\rangle_L$ and to $p \approx 3/16$ for the other 4 states. After each fluorescence readout we proceed to the next measurement conditional on the dark measurement result otherwise we restart the experimental sequence. This choice is made using real time decisions implemented using a field-programmable gate array (FPGA).

A sample of a full pulse sequence for our experiments is shown in Extended Data Fig. 2. Each experiment starts by cooling the ion's three modes of oscillation, using a sequence of precooling, Doppler cooling and electromagnetically induced-transparency cooling. This is followed by pumping of the axial motional mode into a squeezed state, using a pulsed scheme where we typically use around 20 cycles[22]. In order to prepare the $|0\rangle_L$ from the created squeezed vacuum state, we use two modular measurements (Mod(l)) each consisting of an SDF pulse splitting up the oscillator into two components and separating them symmetrically by a distance l and a short fluorescence readout of about 60 μs. The decision whether or not to restart the experimental sequence dependent on the bright or dark detection result takes around 50 μs. The second line of the pulse sequence in Extended Data Fig. 2 shows how $|\phi_+\rangle_L$ is created from $|0\rangle_L$ using the $\hat{U}_L^X(\pi/2, \pi/2)$ operation which requires an appropriate carrier $\pi/2$-rotation, a shorter SDF and a corrective unconditional shift. Then the T-gate is applied and finally the Pauli $\hat{X}_L$ operation is read out. This sample pulse sequence is used during the process tomography experiment for the T-gate. All experiments rely on pulse sequences of the same tools combined in different ways.

Process tomography. We create the six input states described in the previous section and reconstruct their state via readout in the three Pauli bases: $\hat{\rho}_L^{\,j} = \sum_k o_{jk}\hat{\sigma}_k$, where j labels the input state number, k the Pauli basis element and o_{jk} correspond to the readout results (where we added $o_{j0} = 1/2$ for the identity basis element). Then we apply the process of interest to each input state and reconstruct the output state in the same way with λ_{jk} the corresponding measurement results. An arbitrary physical process connecting input states to output states can be expressed in the Pauli basis introducing the process matrix χ: $\mathcal{E}(\hat{\rho}_L^{\,\mathrm{in}}) = \hat{\rho}_L^{\,\mathrm{out}} = \sum_{mn}\hat{\sigma}_L^m\hat{\rho}_L^{\,\mathrm{in}}\hat{\sigma}_L^n\chi_{mn}$. A linear set of equations for the matrix elements of χ_{mn} connects o_{jk} to λ_{jk}: $\boldsymbol{\lambda} = \beta\boldsymbol{\chi}$ with the matrix β calculated from the input state measurements o_{jk}. The process matrix χ is Hermitian and non-negative definite. To ensure these properties we parametrize $\chi = \hat{T}^\dagger\hat{T}$ with

$$\hat{T} = \begin{pmatrix} t_1 & 0 & 0 & 0 \\ t_5 + it_6 & t_2 & 0 & 0 \\ t_{11} + it_{12} & t_7 + it_8 & t_3 & 0 \\ t_{15} + it_{16} & t_{13} + it_{14} & t_9 + it_{10} & t_4 \end{pmatrix} \tag{5}$$

a tridiagonal matrix[43]. We find four more constraints on the elements of $\hat{T}$ following from trace preservation of the logical process[44]. Ensuring these constraints we find the t_i elements which minimize $|\beta\boldsymbol{\chi} - \boldsymbol{\lambda}|^2$ using the NMinimise function of Mathematica.

The method of process tomography is independent of the chosen grid state encoding. We solely specify the methods of input state creation and state tomography, and analyse how well the implemented processes realize logical single-qubit operations. Nevertheless we have additional knowledge about our code states and logical readout and see that a number of effects are not accounted for in process tomography. For example, the logical $\pi/2$-rotation around the Z axis transforms logical $\hat{Y}_L$ readouts to $\hat{X}_L$ readouts. In this case we expect the readout levels to increase: and even though in this particular case our realization of the logical qubit improves, this will lead to infidelities in the process matrix.

Rescaling of the readout directions in order to account for such imprecision is not trivial, because the rotations implemented by gate teleportation typically change the underlying states (that is, they result in more squeezed components or spread out squeezed states), which in general also changes the logical readout level.

In order to understand the level of process fidelity decrease due to such effects, we calculate the process matrix for the ideal process on the ideal approximate code states with the experimentally used number of components and parameters l and r. From this we calculate the fidelity due to the approximation $F_{\hat{O}}^{\mathrm{App.}}$. Further, to assess susceptibility to dephasing of our oscillator, we simulate the process tomography experiment using the typical level of dephasing present in our experiment, and again estimate a fidelity $F_{\hat{O}}^{\mathrm{Sim.}}$. We observe that for the Pauli operations all features related to the approximate code states drop out in the process tomography. Additionally, since the displacement operation is relatively fast, the effects of motional dephasing are minimal compared to that incurred during state preparation and thus this does not influence the process tomography result. For the teleported operations the duration is longer, and the readout axes are interchanged. In this case, we find that $F_{\hat{T}_L}^{\mathrm{App.}} = 96\%$, $F_{\hat{T}_L}^{\mathrm{Sim.}} = 93\%$, $F_{\hat{R}_L^X(-\pi/2)}^{\mathrm{App.}} = 94\%$, $F_{\hat{R}_L^X(-\pi/2)}^{\mathrm{Sim.}} = 91\%$, $F_{\hat{R}_L^Z(-\pi/2)}^{\mathrm{App.}} = 93\%$, $F_{\hat{R}_L^Z(-\pi/2)}^{\mathrm{Sim.}} = 89\%$. The differences between these values and the experimental fidelities are probably due to mis-calibration.

Logical qubit lifetime. Traditionally two-level qubits are characterized by two timescales: T_1, the time in which the higher energy state decays; and T_2, the time

in which a superposition of the two levels dephases. For the logical grid state qubit the notion of these two timescales is blurred since the underlying physical states are not given by a two-level system. In order to measure a timescale relating to T_1, we prepare $|0\rangle_L$ and wait for a variable time after which we measure $\hat{Z}_L$. Results of this measurement as a function of the wait time are shown in Extended Data Fig. 3a along with a fit using an exponential decay $Ae^{-t/T}$ with fitting parameters A and T. In this measurement we find $T = 3.7 \pm 0.2$ ms. Unlike an energy level qubit this measurement does not decay completely to the other level. Instead we end up in an equal superposition more like a traditional measurement of T_2. In the grid state encoding the Hadamard operation can be implemented as a rotation of phase space by $\pi/2$ (and scaling if $l \neq \sqrt{2\pi}$). This is trivially implemented by updating the readout directions and scaling in our classical control system. In this sense the typical sequence to measure T_2 involving preparing $|0\rangle_L$, applying the Hadamard operation, waiting for a fixed duration t and subsequently using an additional Hadamard operation followed by readout of $\hat{Z}_L$ simplifies to the previous experiment. Thus T_1 and T_2 are essentially the same parameters in the grid state encoding.

Nevertheless we can analyse the lifetime of our qubit with a second measurement, we prepare $|+\rangle_L$, wait for a duration t and read out $\hat{X}_L$. This can also be viewed as an analogue of a Ramsey T_2 measurement. The results of this measurement together with the exponential fit are shown in Extended Data Fig. 3b. A similar timescale of $T = 3.6 \pm 0.3$ ms is extracted from the fit.

We can compare these logical qubit lifetimes to the decay of our averaged stabilizer readouts $\hat{S}_X$, $\hat{S}_Z$, which we measure for both states, $|0\rangle_L$, $|+\rangle_L$. The results and timescales are given in Extended Data Fig. 3c–f. We see that the stabilizer readouts decay on shorter timescales than the Pauli readouts.

Two qubit gates on encoded qubits. The tools presented in the main text can be used to perform a two qubit gate on two logical qubits stored in two motional modes of a single ion. Let us assume that we have a single ion and prepared logical grid qubit states $|Q_1\rangle$, $|Q_2\rangle$ in two of the three modes of oscillation. Let us further assume that we manipulated both these modes via the internal ancillary qubit levels $|0\rangle \leftrightarrow |1\rangle$. Then we can implement the circuit given in Extended Data Fig. 4 which realizes a $\hat{\sigma}_L^i$-controlled-$\hat{\sigma}_L^j$ operation using carrier rotations and SDF pulses as well as unconditional displacements. In our current experimental system only the axial motional mode has sufficiently long coherence time to prepare and manipulate grid qubit states. Thus before we can implement such a gate we need first to improve our trap stability.

An alternative method which is more applicable to performing quantum error correction would be to utilize the Coulomb coupling between local modes of two ions held in separate potential wells. This could be used in order to implement a SWAP-gate operation[29–31]. Such a SWAP operation could be used to perform a non-destructive readout of error information from a grid-state qubit in the following manner. First, the encoded oscillator qubit is swapped to the (quasi-)local mode of the ion stored in the neighbouring well by resonant exchange. Second, a carrier rotation together with a state-dependent force pulse is applied to the second ion which transfers part of the syndrome information into that ion's internal state. This could for instance constitute one bit of information required for a phase-estimation protocol[10]. Third, the SWAP operation is repeated, transferring the encoded qubit back to ion 1. This procedure extracts one bit of relevant error information from the encoded grid qubit into the internal states of ion 2. Fourth, the oscillations of the two ions are detuned from each other such that fluorescence readout can be performed on ion 2 without destroying the encoded state in ion 1 (crosstalk of the internal states could be prevented by using ions of two species). For the next relevant bit of information the same procedure is repeated using a different carrier rotation setting. Multiple internal levels of the second ion could be used in order to readout more than one bit of information per swap cycle. The extracted information provides information on the oscillator shift up to a certain precision. Error recovery could then be performed by applying the opposite shift using an appropriate tickling pulse to the encoded qubit.

Data availability

The data that support the plots within this paper and other findings of this study are available from the corresponding authors upon request.

34. Ketterer, A. *Modular Variables in Quantum Information*. PhD thesis, Univ. Sorbonne Paris Cité and Univ. Paris Diderot (2016).
35. Kienzler, D. *Quantum Harmonic Oscillator State Synthesis by Reservoir Engineering*. PhD thesis, ETH Zürich (2015).
36. Wineland, D. J. et al. Experimental issues in coherent quantum-state manipulation of trapped atomic ions. *J. Res. Natl Inst. Stand. Technol.* **103**, 259–328 (1998).
37. Kienzler, D. et al. Quantum harmonic oscillator state control in a squeezed Fock basis. *Phys. Rev. Lett.* **119**, 033602 (2017).
38. Wolf, F. et al. Motional Fock states for quantum-enhanced amplitude and phase measurements with trapped ions. Preprint at http://arxiv.org/abs/1807.01875 (2018).
39. Gerritsma, R. et al. Quantum simulation of the Klein paradox with trapped ions. *Phys. Rev. Lett.* **106**, 060503 (2011).
40. Zähringer, F. et al. Realization of a quantum random walk with one and two trapped ions. *Phys. Rev. Lett.* **104**, 100503 (2010).
41. Gerritsma, R. et al. Quantum simulation of the Dirac equation. *Nature* **463**, 68–71 (2010).
42. Efron, B. & Tibshirani, R. J. *An Introduction to the Bootstrap* (Chapman & Hall/CRC, Boca Raton, 1993).
43. James, D. F. V., Kwiat, P. G., Munro, W. J. & White, A. G. Measurement of qubits. *Phys. Rev. A* **64**, 052312 (2001).
44. Bhandari, R. & Peters, N. A. On the general constraints in single qubit quantum process tomography. *Sci. Rep.* **6**, 26004 (2016).

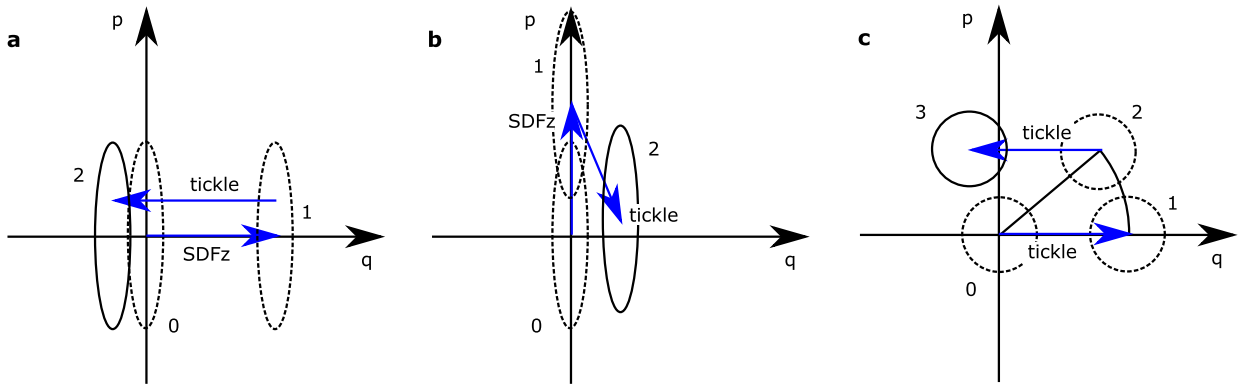

Extended Data Fig. 1 | Calibration techniques in phase space. Here we show how the required properties of the tickling pulse are determined ('calibrated') and the use of the tickling pulse for motional frequency calibrations. **a**, Matching of the tickling pulse to the SDF pulse (see Methods for nomenclature). The squeezed ion motional state (dashed state labelled 0) is displaced using an SDF together with two $\pi/2$ internal state rotations (SDFz). This realizes the displaced squeezed state 1. A subsequent tickling pulse is calibrated in order to revert the displacement implemented by the laser. After this shift the oscillator is in state 2. Whether or not the squeezed state returns to the squeezed vacuum can be probed using the squeezed basis analogue of the red sideband[22]. Shown is the case of a laser displacement along the squeezed axis, which enhances sensitivity for the tickling coupling strength. **b**, Similarly, a laser displacement perpendicular to the squeezed axis is used to calibrate the direction of the tickling pulse. **c**, Motional frequency calibration. The ion is ground state cooled (0), then a coherent state (1) is created by a first tickling pulse. The state evolves freely during the wait time T and rotates by an angle $T\delta$, with δ the detuning from the angular motional frequency ω_m. A second tickling pulse inverts the first displacement. Because of the detuning, the final state (3) does not return to the ground state, which can be detected applying a red sideband probe pulse.

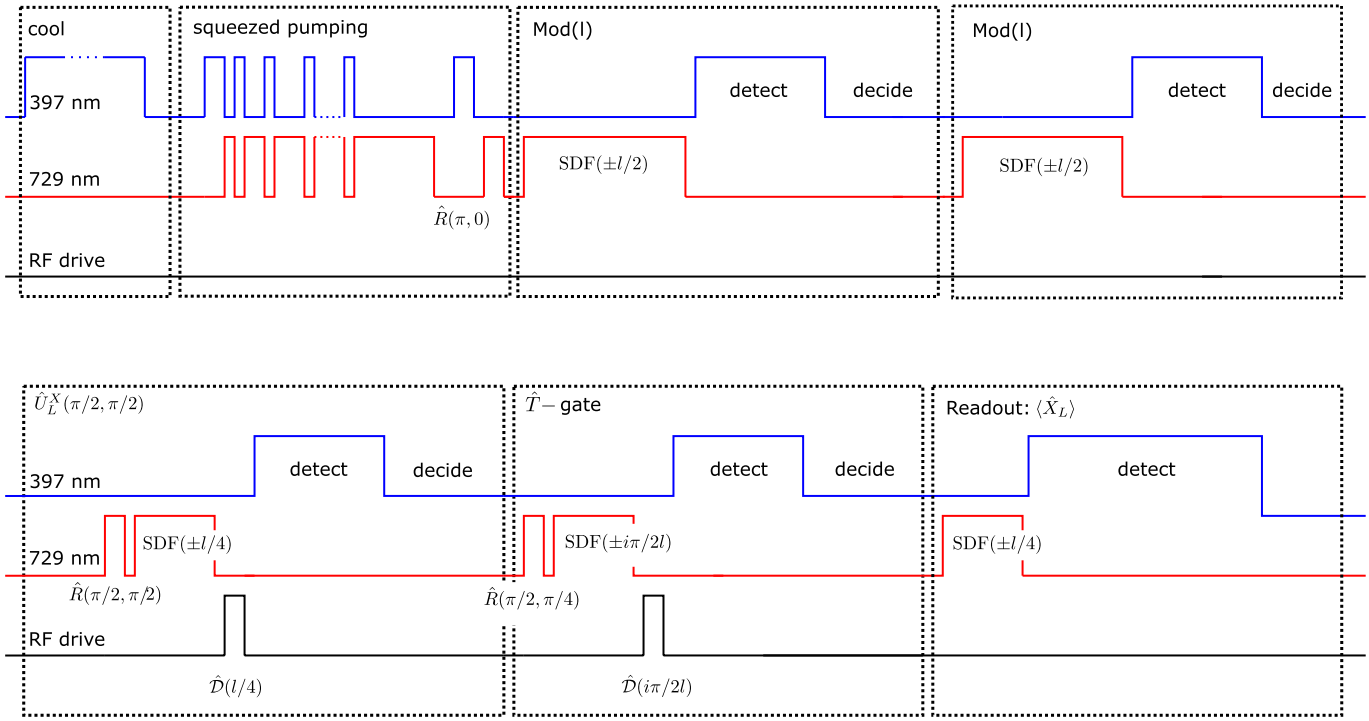

Extended Data Fig. 2 | Example of a pulse sequence. This pulse sequence is used during process tomography of the T-gate. The blue line shows laser pulses based on the 397 nm laser used for cooling and fluorescence detection of the internal states. The red line shows manipulations using the 729 nm laser used for SDF pulses as well as carrier rotations, while the black line denotes tickling pulses implemented using an RF voltage. The upper row shows the sequence used for preparing $|0\rangle_L$, including initial cooling, squeezed state preparation ('squeezed pumping') and modular variable measurements ('Mod(l)'). The lower row shows first the implementation of $\hat{U}_L^X(\pi/2, \pi/2)$ by gate teleportation (creating $|\Phi_+\rangle_L$), followed by application of a teleported T-gate ('$\hat{T}$-gate') and subsequently the readout of the states.

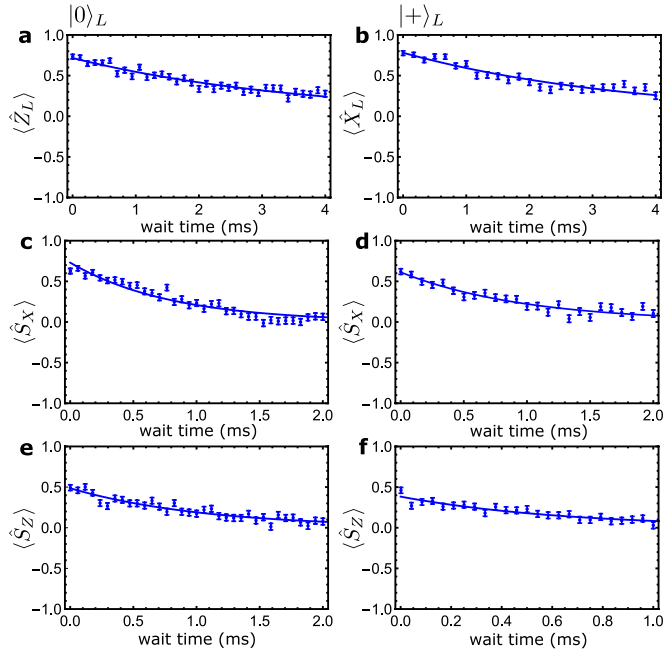

Extended Data Fig. 3 | Grid qubit lifetime measurements. a–f, States are prepared (left column, $|0\rangle_L$; right column, $|+\rangle_L$), and after a variable wait time the state is read out. The resulting measurement data (blue points with s.e.m. error bars) are fitted with an exponential decay $Ae^{-t/T}$ (solid line). For prepared state $|0\rangle_L$: **a**, readout of $\hat{Z}_L$, from which we find $T = 3.7 \pm 0.2$ ms; **c**, readout of $\hat{S}_X$ with $T = 0.8 \pm 0.1$ ms; and **e**, readout of $\hat{S}_Z$ with $T = 1.1 \pm 0.1$ ms. For prepared state $|+\rangle_L$: **b**, readout of $\hat{X}_L$ with $T = 3.6 \pm 0.3$ ms; **d**, readout of $\hat{S}_X$ with $T = 1.0 \pm 0.1$ ms; **f**, readout of $\hat{S}_Z$ with $T = 0.7 \pm 0.1$ ms.

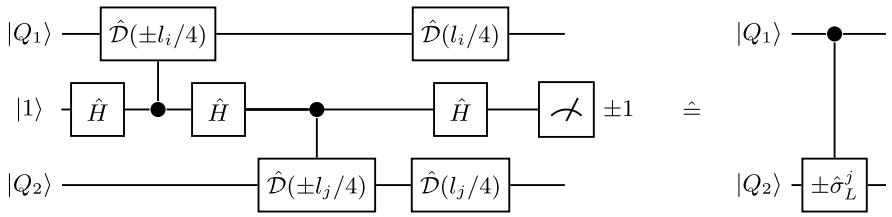

Extended Data Fig. 4 | Two qubit gate implemented in two modes of a single trapped ion. This circuit implements $\hat{\sigma}_L^i$-controlled $\pm\hat{\sigma}_L^j$ operations between two grid state qubits $|Q_1\rangle$ and $|Q_2\rangle$ mediated by one internal ancillary qubit $|0\rangle \leftrightarrow |1\rangle$. The required operations are shown in the left circuit, while on the right the equivalent logical operation is shown. The sign of the operation is determined by the ancillary qubit readout. See Methods for details.

Extended Data Table 1 | Creation of code states

state	figure	creation pulse sequence
$\|0\rangle_L$	1b	(seq 0) $\equiv$ squeezed pumping, Mod(l), Mod(l)
$\|1\rangle_L$	1c	squeezed pumping, Mod(l), Mod(2l)
$\|0\rangle_L$	2a	(seq 0)
$\|1\rangle_L$	2a	(seq 0), $\hat{X}_L = \hat{\mathcal{D}}(l/2)$
$\|+\rangle_L$	2b	(seq 0), $\hat{U}_L^X(0, \text{arb.})$
$\|-\rangle_L$	2b	(seq 0), $\hat{U}_L^X(0, \text{arb.})$, $\hat{Z}_L = \hat{\mathcal{D}}(i\pi/l)$
$\|\phi_+\rangle_L$	2c	(seq 0), $\hat{U}_L^X(\pi/2, \pi/2)$
$\|\phi_-\rangle_L$	2c	(seq 0), $\hat{U}_L^X(\pi/2, \pi/2)$, $\hat{Z}_L = \hat{\mathcal{D}}(i\pi/l)$
$\|0\rangle_L$	4, $\hat{\rho}_L^{\text{in}}$	(seq 0)
$\|1\rangle_L$	4, $\hat{\rho}_L^{\text{in}}$	(seq 0), $\hat{X}_L = \hat{\mathcal{D}}(l/2)$
$\|+\rangle_L$	4, $\hat{\rho}_L^{\text{in}}$	(seq 0), $\hat{U}_L^X(0, \text{arb.})$
$\|-\rangle_L$	4, $\hat{\rho}_L^{\text{in}}$	(seq 0), $\hat{U}_L^X(\pi, \text{arb.})$
$\|\phi_+\rangle_L$	4, $\hat{\rho}_L^{\text{in}}$	(seq 0), $\hat{U}_L^X(\pi/2, \pi/2)$
$\|\phi_-\rangle_L$	4, $\hat{\rho}_L^{\text{in}}$	(seq 0), $\hat{U}_L^X(\pi/2, -\pi/2)$

Left column, code state type. All states used $l \approx 2.5$ while $r \approx 0.9 \approx 7.8$ dB. Middle column, measurement results using this type of state are presented in the given figures of the main text. Right column, pulse sequence used to create the state. Most states use the same initial sequence (seq 0), which is thus defined in the first entry of the table.